We are IntechOpen,
the world's leading publisher of
Open Access books
Built by scientists, for scientists

4,800

Open access books available

122,000

International authors and editors

135M

Downloads

Our authors are among the

154

Countries delivered to

TOP 1%

most cited scientists

12.2%

Contributors from top 500 universities

BOOK CITATION INDEX
CLARIVATE ANALYTICS
INDEXED

WEB OF SCIENCE™

Selection of our books indexed in the Book Citation Index
in Web of Science™ Core Collection (BKCI)

Interested in publishing with us?
Contact book.department@intechopen.com

Numbers displayed above are based on latest data collected.
For more information visit www.intechopen.com

Frequency-Tunable Coherent THz-Wave Pulse Generation Using Two Cr:Forsterite Lasers with One Nd:YAG Laser Pumping and Applications for Non-Destructive THz Inspection

Tadao Tanabe and Yutaka Oyama

Department of Materials Science, Graduate School of Engineering, Tohoku University
Japan

1. Introduction

The development of various original semiconductor devices, which act as electromagnetic wave generators in the THz region of the spectrum, has long been an active area of research in our group. The terahertz (THz) region, which lies between the microwave and infrared regions, offers a wealth of untapped potential. In most cases, the devices are based upon the utilization of THz lattice vibrations in compound semiconductors (*e.g.*, GaP and GaAs), which has recently become an important technology behind frequency-sweepable coherent THz-wave sources, following the invention of the semiconductor laser by Nishizawa in 1957 [1]. In 1963, Nishizawa was the first to predict the utility of the phonon and molecular vibration in semiconductors for optical communication and THz-wave generation. However, an important frequency gap between the microwave and optical frequencies remained, and presently is referred to as the THz region. In 1983, the semiconductor Raman laser was realized, which relied on the longitudinal optical phonon (LO phonon) mode of a GaP crystal. This work highlighted the generation of a 12-THz wave with a peak power as high as 3 W [2]. The output power of the Raman laser was increased by a phonon enhancement effect within the waveguide-structured GaP [3].

A high-power frequency-tunable THz-wave was generated via excitation of phonon–polaritons mode in GaP [4–8]. The frequency range was approximately 0.3–7.5 THz, in which the peak power was greater than 100 mW over most of the tunable region [5–7]. The generated THz-wave power and frequency regions have been shown to depend on carrier densities within the GaP crystals.

Furthermore, THz signal generators have been developed with various functions. Generation of narrow-linewidth THz waves has very useful applications in the fields of high-resolution spectroscopy, optical communications and *in-situ* security screening. The CW THz waves are generated from GaP by using semiconductor diode lasers. The linewidth is about 4 MHz. A 30 cm-long portable THz-wave generator is constructed using two Cr:Forsterite lasers pumped using a single Nd:YAG laser.

In this chapter, we review the photonic approaches of THz-wave sources and highlight the principles and performance of these THz-wave generating devices. Developments in THz

technology allow spectroscopic investigation of low-energy excitations of macromolecules, such as molecular rotations, hydrogen bonding, and intermolecular interactions, with a broad frequency range and high resolution. Indeed, low-energy excitations are believed to be critical in understanding the complex behavior of biological molecules, cells, and tissues. For industrial applications, we have recently developed THz diagnosis technologies. Deformation of polyethylene can be monitored using polarized THz spectroscopy. The THz diagnoses the inside of object even with covered by materials.

THz wave has unique properties with high transparency for non-polarized materials such as with radio waves and easy handling as in the case of light. THz waves are expected to be a promising frequency for the non-destructive diagnosis of the interior of non-polarized materials [9-14]. For the THz inspection method, the spatial resolution is higher compared with that of conventional microwave techniques.

The energy of a THz wave is as low as room temperature, for example, whose energy level corresponds to hydrogen bonding, van der Waals interactions and free carrier absorption. Although the transparency of a THz wave is not as great as that of X-ray, a THz wave is sensitive to soft materials such as hydrate as well as to wet conditions. To date, our group has utilized THz waves for inspections of diffused water and defects in timber and concrete blocks using a 0.2 THz generator [15]. The phase transition of liquid crystal has been investigated based on molecular interactions using a GaP THz signal generator [16]. Polarization THz measurements are helpful for THz non-destructive diagnosis of the tensile strain in deformed UHMWPE [17]. Use of THz waves in conjunction with X-ray and γ-ray measurements shows promise for analysis macro-structures in organic materials and polymers. Recently, compact sized THz wave generators have been developed for practical use [18]. For single-frequency coherent THz waves, a geometrical optical design can be applied. A THz beam spot can be controlled to be as small as the wavelength of a THz wave. Such THz sources are suitable for spectroscopic imaging with spatial high-resolution.

As one application of the THz diagnosis, the study has focused on the interior copper conductors covered with insulating polyethylene. THz reflectivity of the copper surfaces was investigated by using the GaP THz wave generator. Surface evaluation of copper with various conditions was performed using THz diffused reflection spectroscopy. Copper is a basic metal. In particular, copper cables are used for a wide variety of electric components. Confirmation of copper conductors covered with plastics is essential for a social safety. A suitable way to evaluate the deterioration of interior copper conductors has not yet been fully established. A non-destructive method for the diagnosis of electric cables would be of value for quality evaluation in use of it.

2. THz-wave generation from semiconductors

Widely frequency-tunable high-power THz waves have been generated from GaP by pumping with a Q-switched Nd:YAG laser and an OPO, or two Cr:Forsterite lasers [4–7]. THz waves were generated in the frequency range from 0.3 to 7.5 THz using difference frequency generation (DFG) via the excitation of phonon–polaritons in GaP. Indeed, this process converts energy very efficiently, and resulted in a THz wave with an energy of 9 nJ/pulse (peak power of 1.5 W). Furthermore, frequency-tunable CW THz waves were generated by enhancing the power density of incident beams from semiconductor lasers [8].

The THz-wave output power (P_{THz}) can be increased by exploiting the inverse proportion to the beam spot size, S, based on the follow equation:

$$P_{THz} = \frac{A}{S} \cdot P_1 \cdot P_2 \, ,$$

(1)

where A is the coefficient for generating THz waves from a GaP crystal pumped under non-collinear phase-matching conditions. Note that A is estimated to be 0.4×10^{-13} W^{-1} cm^2 [15, 16], while S is the spatial overlap of the cross-sectional areas of the pump and signal beams, and P_1 and P_2 are the effective powers of the pump and signal beams, respectively.

The two lasers used for the DFG of THz waves via excitation of the phonon–polariton mode in GaP crystals were a 1.064 μm Nd:YAG source and a β-BaB_2O_4-based OPO system. They were set up in a non-collinear configuration with a very small angle between the two beams, and the GaP crystals were positioned as depicted in Fig. 1 [4–7]. The wavelength of the pump beam was varied between 1.035 and 1.062 μm, which corresponded to generated THz-wave frequencies between 8 and 0.5 THz. The THz-wave energy can be collected with parabolic reflectors and determined using a pyroelectric DTGS detector operating at room temperature or a liquid-helium-cooled Si bolometer.
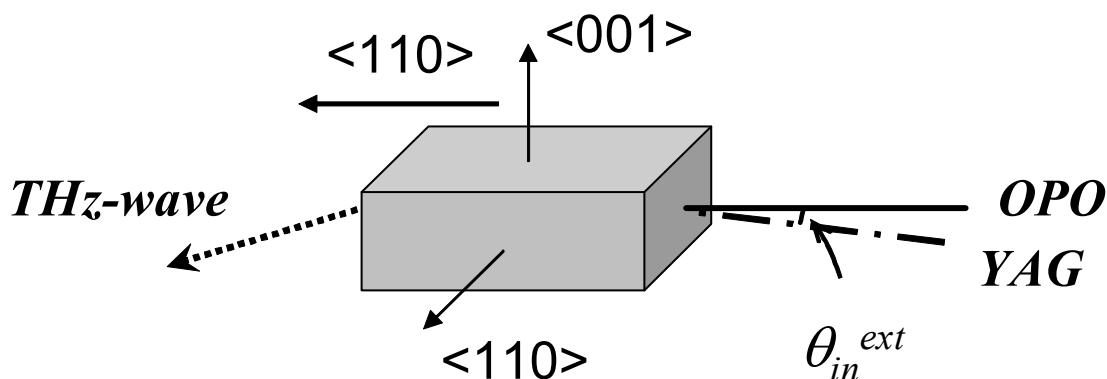

Fig. 1. Schematic of the YAG and OPO beam paths within the GaP crystal.

The THz-wave generation using two Cr:Forsterite lasers (Cr:F) was very similar to the OPO-based system. The pump and signal beams were combined using a cubic polarizer placed on a rotating platform on top of a linear stage, which automatically produced a very small angle between the two beams to fulfill the phase-matching condition and achieve a spatial overlap of the incoming beams. The non-collinear phase-matching was satisfied under the following condition [4, 6]. The calculated angle between the pump and signal light beams (θ_{in}) inside the GaP crystal matched quite well with respect to the experimental results, as long as $\theta_{in} \ll 1$:

$$\frac{\theta_{in}}{v} = \sqrt{\frac{2(\Delta q / q)(n_I^2 / n_L \cdot n_S)}{v_L \cdot v_S}} \, ,$$

(2)

where v_L, v_S, and v are the frequencies of the pump, signal, and THz waves, respectively; $(\Delta q / q)$ is the relative deviation of the wave-vector phonon–polaritons in the GaP crystal; n_I, n_L and n_S are the refractive indexes of the THz wave, pump, and signal beams, respectively;

and Δq is the deviation of q from the exact phase-matching value in the collinear configuration, which can be described as

$$\left(\frac{\Delta q}{q}\right) = \frac{n_I - n_{eff}}{n_I} . \tag{3}$$

In the case of the collinear interaction, the difference between the pump and signal wave numbers can be described by the following equations:

$$k_L - k_S = k = \frac{n_{eff} \cdot 2\pi\nu}{c} , \quad n_{eff} = n_S + \nu_L \cdot \frac{\delta n}{\delta \nu} \tag{4}$$

where k_L and k_S are the wave numbers of the pump and signal beams, respectively, and $\delta n/\delta \nu$ is the frequency dispersion of the refractive index. Moreover, the dispersion relationship of phonon–polaritons in GaP can be given by the following equation:

$$\left(\frac{cq}{2\pi\nu}\right)^2 = n_I^2 = \frac{\left(\varepsilon_S \nu_0^2 - \varepsilon_\infty \nu^2\right)}{\left(\nu_0^2 - \nu^2\right)} , \tag{5}$$

where ε_s and ε_∞ are the static and optical frequency dielectric constants, respectively (ε_s = 11.15, ε_∞ = 9.20), and ν_0 = 11.01 THz is the pure transverse optical phonon frequency [19]. In general, this equation holds true as long as the THz frequency, ν, is not nearly equal to ν_0. The internal angle external to the GaP, θ_{in}^{ext}, is given by the relationship

$$\theta_{in} \approx \frac{\theta_{in}^{ext}}{n_S} , \tag{6}$$

where θ_{in} is calculated to be 0.1° at 2 THz; therefore, the two near-IR beams overlapped sufficiently to interact with each other. The polarization of the pump and signal beams was adjusted to be in the <001> and <1$\bar{1}$0> directions, respectively. Figure 2 illustrates the relationship between θ_{in}^{ext} and the THz-wave frequency at which the maximum output power was obtained. The slope of the curve declined noticeably, which was reflected in the measured dispersion curve of the phonon–polariton branch of GaP. The θ_{in}^{ext} increased with the wavelength of the pump and signal beams, while the propagation direction of the THz wave was related to $(\Delta q/q)$. The output direction of the THz wave depends on the wavelength of the pump and signal beams, as well as the THz frequency. The angle of the propagation direction of the THz wave inside the crystal, θ_I, is given as

$$\sin\left(\theta_I - \theta_{in}\right) = \left(\frac{k_S}{q}\right)\sin\theta_{in} , \quad \text{with } \theta_I \gg \theta_{in}. \tag{7}$$

From this, we obtain

$$\sin\theta_I \approx \sqrt{\left(\frac{2\Delta q}{q}\right) \cdot \left(\frac{\nu_S}{\nu_L}\right) \cdot \left(\frac{n_S}{n_L}\right)} \approx \sqrt{\frac{2\Delta q}{q}} . \tag{8}$$

The THz-wave direction was compensated with a pair of off-axis parabolic reflectors, where one of them was carefully moved on a translation stage. The GaP crystal was rotated at a lower frequency in the Cr:F-based system when compared to the OPO-based source to prevent total internal reflection of the THz wave.
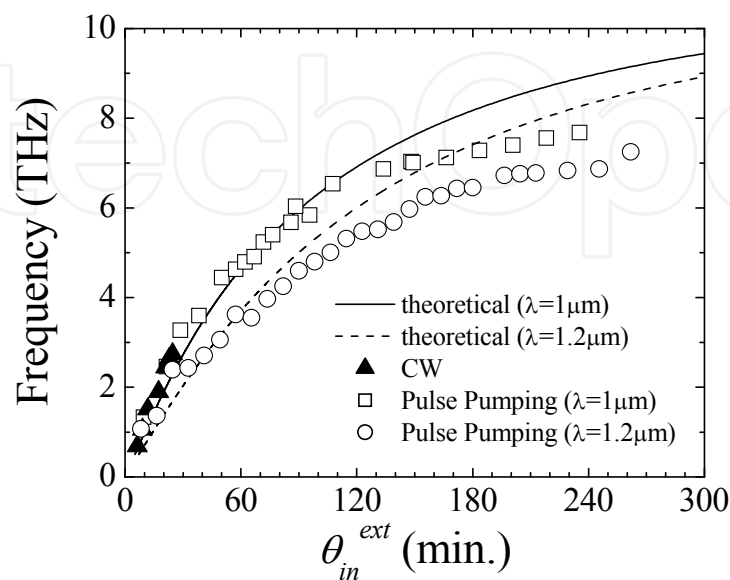

Fig. 2. The relationship between θ_{in}^{ext} and the THz-wave frequency at which the maximum output power was obtained in CW and pulse pumping. The solid line represents the calculated relationship described in more detail within the text.
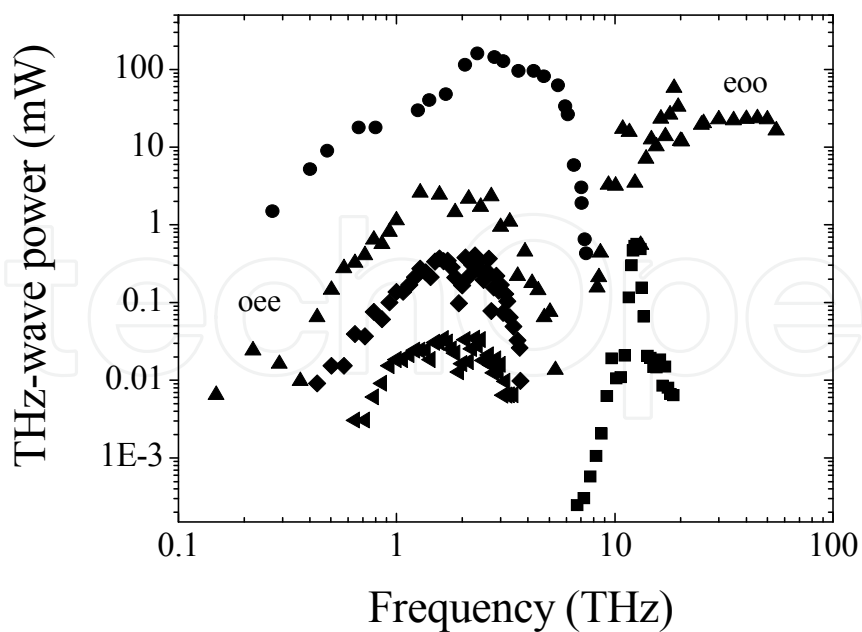
Fig. 3. Frequency dependence of the THz-wave output power from various semiconductor crystals. Note: the pump and signal energy was 3 mJ before incidence to the crystal: GaP (●), GaSe (▲), CdSe (■), ZnGeP$_2$-oee (◆), and ZnGeP$_2$-eoo (◄).

Figure 3 shows the frequency dependence of the maximum THz-wave output power at various θ_{in}^{ext}. The pulse energies of the YAG and OPO were both attenuated to 3 mJ before incidence to the GaP crystal. The THz-wave output power remained stable at approximately 100 mW over a wide frequency range (2.0–5.2 THz). The total tunable frequency range was 0.3–7.5 THz. In cases when the THz-wave frequencies were greater than 5.5 THz ($\theta_{in}^{ext} > 70°$), a much higher power was obtained by rotating the GaP crystal in order to prevent total internal reflection. The THz-wave output power increased linearly with the pump and signal beam energy. Note that the frequency bandwidth is equivalent to the pump and signal beams.

Figure 4 shows the THz-wave power generated as a function of the measured pump beam energy using the Cr:F-based system. It can be seen that the THz-wave power was nearly proportional to the pump energy. When the pump and signal energies were 11.4 and 11.6 mJ, respectively, the THz power increased to 1.5 W for a 10-mm-long crystal without causing surface damage.
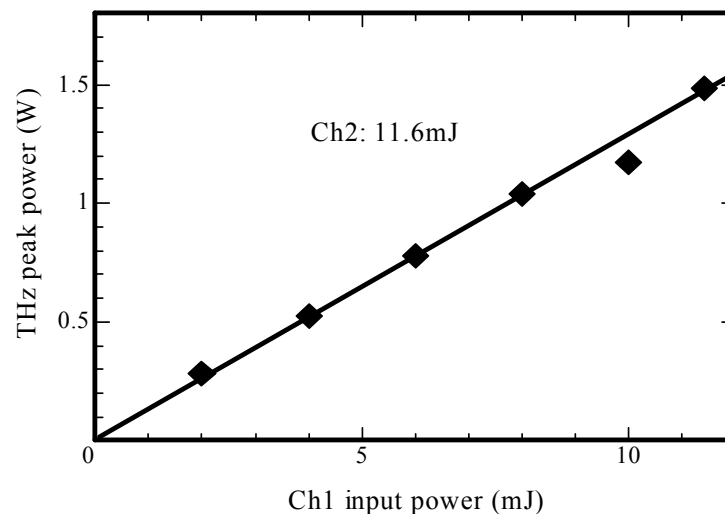

Fig. 4. Generated THz-wave power as a function of the pump beam (Ch1) energy/pulse in the 10-mm-long GaP crystal using a Cr:F source system. The signal beam (Ch2) energy/pulse was 11.6 mJ.

The continuous wave (CW) single-frequency THz waves were generated in a widely frequency-tunable pumping source consisting of an external cavity laser diode (ECLD) and a laser diode (LD)-pumped Nd:YAG laser combined with an ytterbium-doped fiber amplifier (FA) [8]. The estimated THz-wave output peak was 50 pW. In the automatic measurement of transmission spectroscopy, the wavelength of the ECLD was swept from 1.0538 to 1.0541 μm with external cavity fine-tuning. The THz frequency can be shifted according to the wavelength of ECLD. The THz-wave generation efficiency is related to the THz absorption coefficient in GaP crystals. High-power THz-wave output requires a stoichiometric control of the GaP to reduce the THz absorption due to free carriers and phonons in crystal.

In the waveguide structure, efficient THz-wave generation was achieved. THz-wave generation was demonstrated in a GaP waveguide with the same size as the wavelength of THz-wave under a collinear phase-matching condition. The conversion efficiencies of THz wave generation from the rod-type waveguides were estimated. Interestingly, higher

conversion efficiencies were achieved as the waveguide size decreased. For example, in the case in which the waveguide cross section was 200 μm × 160 μm, the conversion efficiency increased to 7.6×10^{-12} W^{-1}. This value was an order of magnitude greater than that in bulk GaP crystals (7.4×10^{-13} W^{-1}).

In addition to the GaP crystal measurements, we also generated frequency-tunable coherent THz-waves using GaSe, $ZnGeP_2$, and CdSe semiconductors based upon difference-frequency generation. GaSe had a high second-order nonlinear optical (NLO) coefficient (d_{22} = 54 pm/V) [20]. Furthermore, GaSe crystals have merit because they can be used to construct a simple THz-wave generation system, since collinear phase-matched DFG eliminates the complexity of angle-tuning in both the input and output beams. THz waves were generated in a wide frequency range from the THz to the mid-infrared region as shown in Fig. 3. Note that Fig. 3 shows the frequency dependence of the THz-wave output power from each semiconductor crystal at various PM angles using the YAG and OPO-based sources. Upon closer inspection of Fig. 6, it is apparent that the combination of GaP (0.3–7.5 THz) and GaSe (10–100 THz) had the widest tunable range with the highest power.

In practical applications, THz-wave generation systems have been used for spectroscopic measurement and THz imaging. A portable THz-wave generator is necessary for practical use, by which it can be moved closer to sample for THz sensing in the field. For example, in organic and inorganic crystal fabrication processes, crystalline defects can be detected using a THz spectrometer. For this motivation, using only one small 30-cm-long Nd:YAG laser and two Cr:Forsterite crystals, we constructed two Cr:Forsterite lasers pumped with the YAG laser and generated THz waves with the compact device. We investigated the pulse duration and delay time to realize Cr:Forsterite lasers which are suitable for use as the THz-wave generator because it requires overlapping of two Cr:Forsterite laser pulses both temporally and spatially for DFG in GaP.

A Cr:Forsterite ($Cr:Mg_2SiO_4$) laser is a solid state laser that is tunable between 1130 and 1370 nm. The laser properties have been investigated, leading to the CW and mode-locked pulse operations. A Cr:Forsterite crystal has Cr^{4+} in the tetrahedrally coordinated Si^{4+} site, which acts as the lasing ion. Crystal growth processes induce impurities such as Cr^{3+} and Cr^{2+}. Those impurities can be decreased by annealing. Two Cr:Forsterite crystals (Cr:F-1, Cr:F-2) with different crystal properties were used for this study: Cr:F-1 is dark blue and Cr:F-2 is dark green. Respectively, they are a rectangular parallelepiped (-R) and a Brewster-cut crystal (-B) of 5 mm × 5 mm (cross-section) × 10 mm (length). Transmittance spectra of Cr:F-1 and Cr:F-2 were measured in the NIR region at room temperature and the absorption coefficient were estimated, respectively. The absorption peaks at 550, 660, 740, and 1060 nm are attributed to the Cr^{4+}. In contrast, Cr^{3+} has absorption at 474 and 665 nm. At around 700 nm, the Cr^{3+} absorption is dominant compared to that of the Cr^{4+}. The 732-nm absorption is considerably higher than that at 1064 nm, but the slope efficiency excited at 732 nm is less than 1064 nm. Consequently, a Nd:YAG laser was used for pumping Cr:Forsterite. The figure of merit (FOM) of Cr:F-1 and Cr:F-2 are 8.0 and 5.9, respectively. A Q-switched Nd:YAG laser with 10-ns pulse duration at 10 ~ 30Hz repetition was used to pump the Cr:Forsterite crystals. Selective frequency cavity oscillator systems were constructed using the Cr:F-1 and Cr:F-2. The Cr:Forsterite laser characteristics of the pulse duration and delay time were measured in terms of the Cr:Forsterite laser energy and cavity length. A THz-wave generation system was constructed using two Cr:Forsterite crystals and one Q-switched Nd:YAG laser. A plane-plane cavity oscillator was constructed for measurement of the slope efficiency in the Cr:Forsterite laser. The output coupler is of 6% transmittance around 1.2 μm. The Cr:Forsterite

laser energies using Cr:F-1-B, Cr:F-1-R, and Cr:F-2-B were measured according to changes in the Nd:YAG laser energy. Cr:F-1-B has the highest slope-efficiency of 8.4%, with the lasing threshold of 2.2 mJ/mm². Slope efficiencies and lasing thresholds are respectively 6.8%, 2.0 mJ/mm² in Cr:F-1-R and 4.8%, and 4.6 mJ/mm² in Cr:F-2-B. These results suggest a relation of the slope efficiency to FOM and the crystal shape.

It is necessary to select a frequency for THz-wave generation. The cavity oscillator using a diffraction grating can select a frequency. The selective-frequency cavity was adjusted so that the first-order reflected light is directed to the direction of incident beam. The cavity can oscillate at 1250 nm when the incident beam angle is 31.2° normal to the grating of 830 lines/mm. The selective frequency Cr:Forsterite laser can be outputted from zero-order light. The pulse duration and delay time were optimized as a function of Cr:Forsterite laser energy and cavity length. The laser crystal was Cr:F-1-R. The delay time was measured as the time from the 50% rising edge of the Nd:YAG laser to the 50% rising edge of the Cr:Forsterite laser using photodiodes and an oscilloscope. The 200 points were recorded at the same optical condition; each result was plotted and fitted to a Gaussian function for measurement of the pulse duration and delay time.

Figure 5 shows the Cr:Forsterite laser characteristics of the pulse duration and delay time when the cavity length was fixed at 20 cm. The Nd:YAG pumping laser energy is changed to 66 mJ, 80 mJ, and 95 mJ. Changing the optical alignment at each Nd:YAG laser pumping
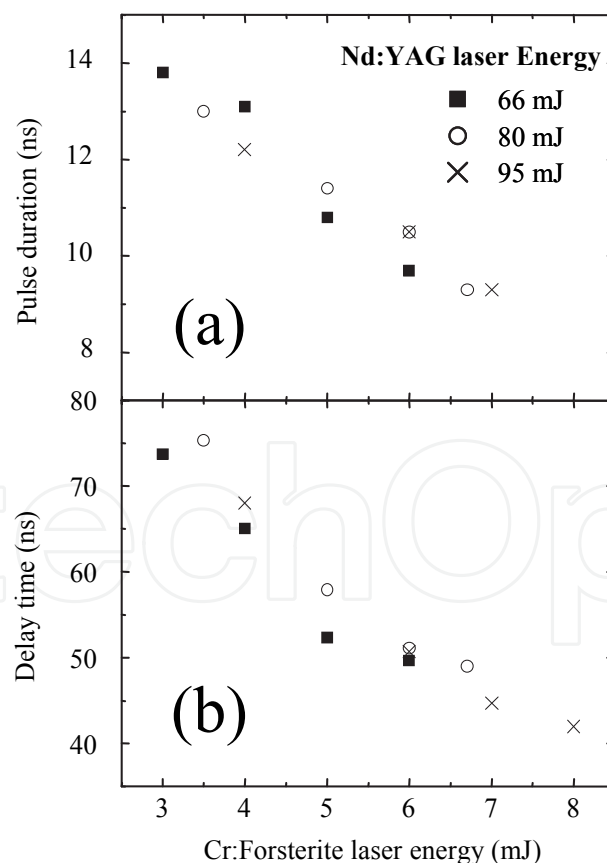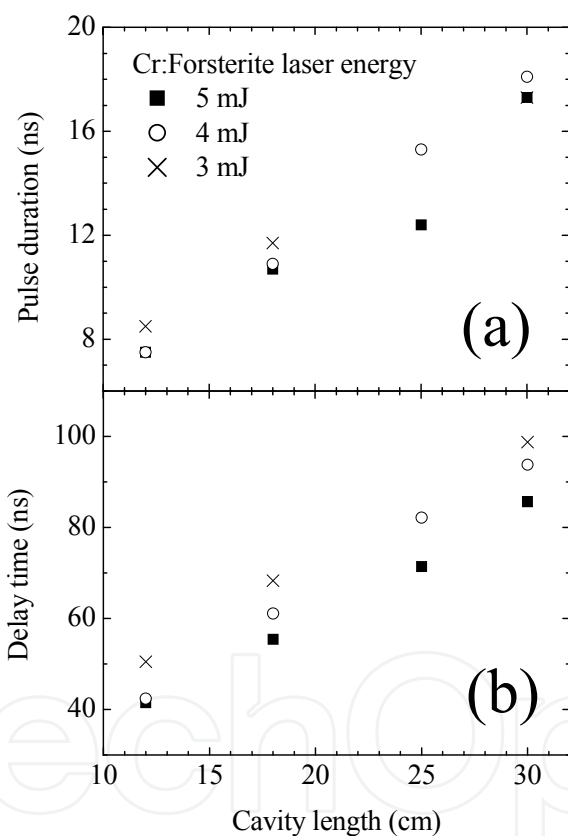

Fig. 5. Cr:Forsterite laser characteristics of the pulse duration (a) and delay time (b) at Cr:Forsterite laser energy of 3–8 mJ. The cavity length was fixed to 20 cm. Nd:YAG laser power was changed to 66 mJ, 80 mJ, and 95 mJ.

energy changed the Cr:Forsterite laser energy to maximum. Both the pulse duration and delay time are decreased when the Cr:Forsterite laser energy increases.

Figure 6 shows Cr:Forsterite laser characteristics of the pulse duration and delay time for the case in which the cavity length was changed from 12 cm to 30 cm at Cr:Forsterite laser energy of 3 mJ, 4 mJ, and 5 mJ. Both the pulse duration and delay time are increased as a function of the cavity length. The result of pulse duration at any cavity length can be understood according to the photon lifetime, which is

$$\tau = \frac{2L}{c(1-R)}$$

(9)

where τ is the photon lifetime, L is the cavity length, c is the velocity of light, and R is the transmittance of an output coupler. Therefore, the cavity length produces a long photon lifetime and long pulse duration.

Fig. 6. Cr:Forsterite laser characteristics of the pulse duration (a) and delay time (b) with the cavity length of 12–30 cm. The Cr:Forsterite laser energy was 3 mJ, 4 mJ, and 5 mJ.

According to these results, the delay time can be controlled according to the Cr:Forsterite laser energy and cavity length. The Cr:Forsterite laser energy is controllable according to the conversion efficiency and pumping energy. The conversion efficiency is changed by optical alignment. Each pumping energy of the two Cr:Forsterite lasers can be changed using a pair of a polarizer and a half-wavelength plate, even if single Nd:YAG laser is used. The method can generate a higher-powered THz wave because the two laser conversion efficiencies are kept high.
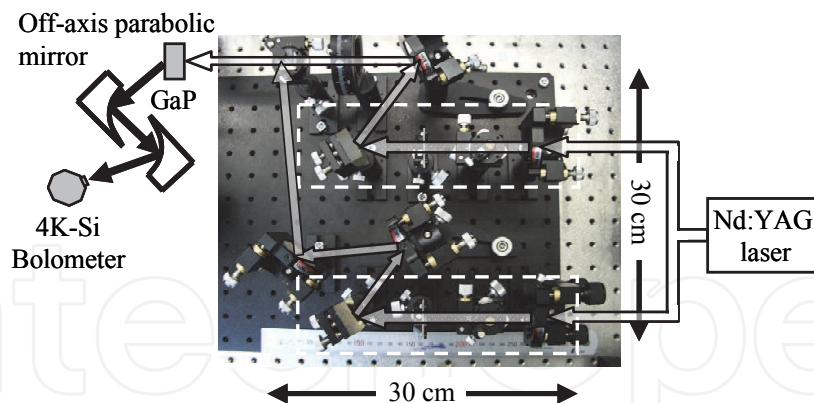
Fig. 7. Optical setup of THz-wave generation with two Cr:Forsterite lasers. The THz-wave detector was a liquid-He cooled silicon bolometer.

Figure 7 shows that two Cr:Forsterite laser oscillators with a 15-cm cavity for THz-wave generation were constructed to be 30 cm × 30 cm. The 30 cm-length Nd:YAG laser can be put diagonally under this Cr:Forsterite laser system. The two different frequency lasers were generated respectively using Cr:F-1-R and Cr:F-2-R with single Nd:YAG pumping of 95 mJ and 105 mJ. The Cr:Forsterite laser using Cr:F-1-R crystal energy is 5.0 mJ; the frequency is tuned to around 1238.4 nm. The Cr:Forsterite laser using Cr:F-2-R crystal energy is 1.5 mJ and the frequency is 1223.5 nm. The two pulses are overlapped temporally and spatially at the GaP crystal surface. The pulse timing was tuned using the conversion efficiency of Cr:Forsterite laser. The THz wave was generated with energy of 4.7 pJ around 2.95 THz. Both the Cr:Forsterite laser line widths were measured as less 0.07 nm using a spectrum analyzer. The linewidth of the generated THz wave is estimated as less than 30 GHz.

Changing the conversion efficiency and pump energy of a Cr:Forsterite laser controlled temporal overlap of two Cr:Forsterite laser pulses. A THz wave was generated using two Cr:Forsterite lasers pumped using a single Nd:YAG laser. The Cr:Forsterite laser system was built as 30-cm square for portable use in the field.

3. Polarized THz spectroscopy for uniaxially deformed ultra high molecular weight polyethylene

One research objective is developing THz evaluation technique of uniaxially deformed polyethylene. Polarized THz spectra have been measured for the deformed polyethylene at room temperature. The THz pulse has a linear polarization.

Ultra high molecular weight polyethylene (UHMWPE) has strength against impact force, friction, chemical attack, and coldness. Therefore this material has been used for many industrial applications, for example gears, gaskets and artificial joints. Several non-destructive tests for UHMWPE have been developed already. The conventional methods are XRD, FT-IR, Raman spectroscopy. These methods should be improved for easy and safe test of mechanical deformation of bulk polymer. The molecular vibration modes of polyethylene are well known. The 14 vibration modes of polyethylene are divided into two types: carbon – carbon vibration and CH_2 plane vibration. In THz spectra of UHMWPE, absorption band is appeared around 2.2 THz, which is assigned to B_{1u} translational lattice vibration mode [21, 22]. THz wave has high transparency for polymers comparing to mid-infrared. Furthermore,

it is harmless and easy to use it. Until now, chemical degradation diagnosis of UHMWPE was reported with THz Time Domain Spectroscopy [23]. THz spectra have been obtained for γ-ray irradiated UHMWPEs with or without vitamin E doping. Vitamin E has anti-degradation effect on UHMWPE.

The UHMWPE plates were deformed at room temperature. One day after deformation, the polarized spectra were obtained with every strain. The measurement frequency is swept from1.5 to 3 THz with 15 GHz step. It takes about 10 minutes for measurement. The 2.2 THz absorption band is due to B_{1u} lattice translational vibration mode of PE. For the spectra with the polarized direction of THz wave parallel to the deformed direction, the absorbance decreases drastically as a function of strain. For the spectra with the THz wave direction perpendicular to the deformed direction, the absorbance decreases gradually in the perpendicular direction.

The integral absorption intensities of the 2.2 THz band are plotted as a function of strain in Figure 8(a). In the parallel direction, up to 25% strain, absorption intensity decreases rapidly. Over 25% strain, the intensity decreases slowly. The degrees of orientation are estimated from XRD. In figure 8(b), the THz absorption intensities in parallel direction are plotted against the degrees of orientation from XRD. This relative is appeared linearity. This result indicates the correlative between THz spectroscopy and XRD. These results suggest the absorption intensity decrease of parallel polarization is caused by orientation.
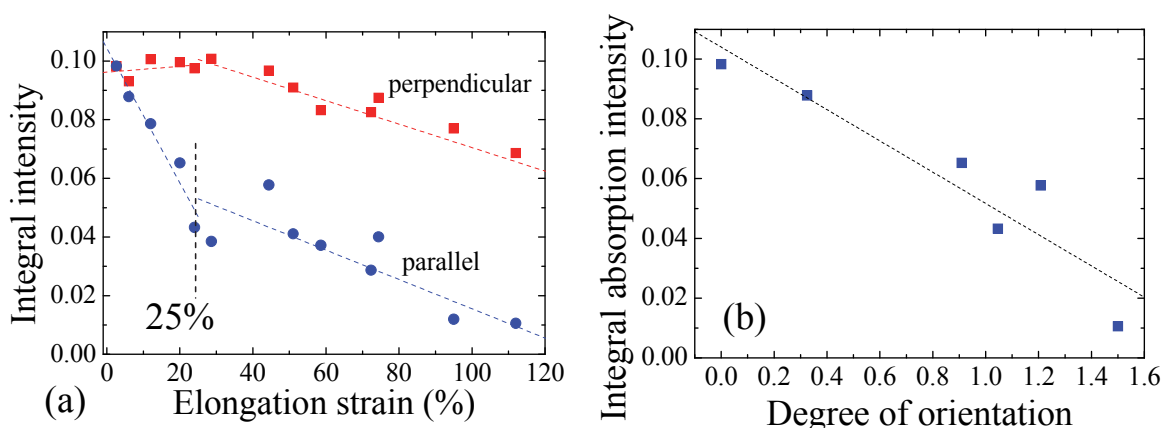

Fig. 8. (a) The integrated absorption intensities of the B_{1u} band as a function of the degree of elongation strain. Incident THz wave was polarized parallel (●) and perpendicular (■) to the axial direction of the deformation. (b) THz absorption intensity vs. degree of orientation. THz wave electric polarization direction is perpendicular to the deformation direction. Degree of orientation was evaluated by XRD measurements.

These results are discussed with lamellar model. Dependent of THz spectral feature on the polarization direction as well as strain amount is explained. THz absorption intensities are inversely proportional to the degree of orientation. When lamellas are oriented along c-axis, the dipole moment direction of B_{1u} vibration mode is perpendicular to c-axis. Then, the B_{1u} absorption band cannot be observed with THz wave polarization direction to the c-axis. According to the IR selection rule, absorption intensity decreases in the parallel polarization spectrum.

For *in-situ* spectroscopic measurements of UHMWPE during uniaxial deformation, the UHMWPE plate was strained at every 10 minutes with 1 % step. It is appeared that the red
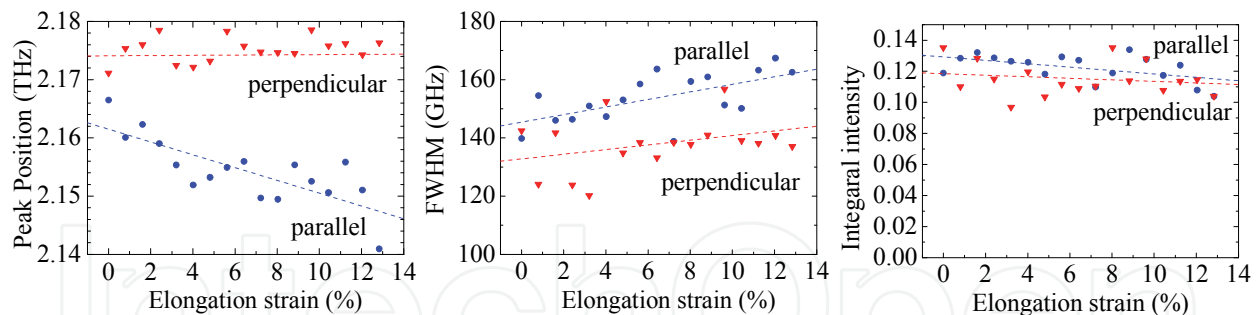
Fig. 9. The absorption peak position, FWHM, and integral absorption intensity of the B_{1u} band as a function of the degree of elongation strain.

shift and widening of B_{1u} absorption band as a function of strain. For perpendicular polarized spectra, the clear peak shift and widening are unclear. For the 2.2 THz band, the absorption peak position, full width at half maximum (FWHM) and integral absorption intensity are plotted in Figure 9 against the elongation strains, respectively. The peak position clearly shifts to lower frequency in the parallel polarized *in-situ* spectra. The peak shift rate is -7.6 % / strain. For absorption bands in higher frequency regions, Richard Wool and co-researchers reported that the peak shift rates of the CH_2 rocking B_{1u} band at 730 cm^{-1} and the CH_2 B_{2u} bending band at 1472 cm^{-1} are -3.0 % and -0.6 % / strain, respectively [24]. The relation between the peak shift rate and peak position is appeared linearity in Figure 10.
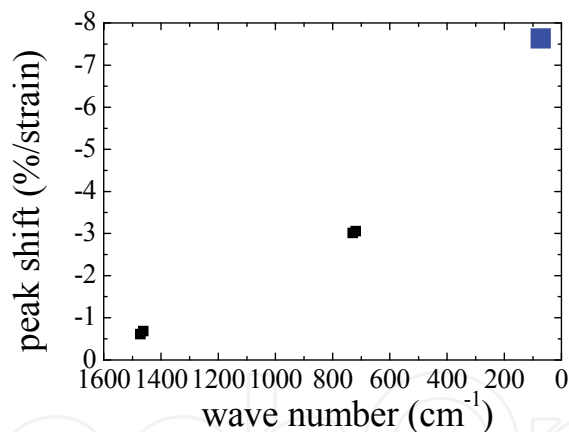

Fig. 10. The relation between peak shift rate and peak position of the B_{1u} band during uniaxial deformation.

Polarized THz wave spectra were obtained for evaluation of polymer chains in mechanically extensional-deformed UHMWPEs. THz absorption band was seen around 2.2 THz which is due to the B_{1u} translational lattice vibration mode. For the deformed UHMWPE, the dichroism is appeared in the 2.2 THz band intensity and peak position. The absorption intensity is smaller in spectra with the THz wave electric polarization direction parallel to the deformation direction than that with the polarization direction perpendicular. The peak position shift and absorption intensity is dependent on the amount of elongation strain, respectively. Based on these results, it is suggested that the THz nondestructive diagnosis of the tensile strain in deformed UHMWPE is possible based on the dichroism of B_{1u} band intensities on polarized THz wave spectroscopy.

4. THz reflection spectroscopy for metal conductor surfaces covered with insulating polyethylene

The THz wave has a lot of characteristics, for example, high permeability for non polar materials, less-invasive, high reflectance on metal surfaces and safety. Our one research target is a THz application for monitoring of metal surface corrosion. Even a metal surface has a corrosion protective covering for practical uses, THz wave is transparent for covering polymers. Here at the metal surface THz wave is absorbed due to corrosion products. This application has many merits as following, high spatial resolution comparing to that of conventional microwave techniques, non-contact, non-destructive and safety.

Until now, the THz spectral data base has been developed mainly for organic materials. That data for metal and inorganic materials is under construction. However, of course, for THz non-destructive applications, the THz spectral data of metal compounds is very important. THz characteristics of metal compounds are essential. We have focused on copper for the non-destructive THz inspection of electric power lines. At present, inspection method of electric cupper cable is based on pealing of cover with visual observation. For prevention of unexpected break down, the non-destructive inspection is desired as a THz application. The non-destructive THz inspection can be applied even for live power lines. Thus THz spectra have been measured for inorganic chemicals of copper, such as Cu_2O, CuO, $Cu(COO)_2 \cdot 1/2H_2O$. THz reflection spectrum of natural cupper oxides on an electric line surface was measured for practical applications. The difference of spectral features between standard copper chemicals and natural copper oxides has been discussed.

For sample preparation, Cu_2O, CuO and Copper oxalate were purchased with 99 % purity. These samples were formed into pellets with PE powder under various concentrations for transmittance THz spectral measurements. The PE powder has high permeability for THz wave. Sample and PE powder are mixed and pressed, then a 1 mm thickness PE pellet was prepared with the diameter of 20 mm. In order to escape the interference in THz spectral measurements, the pellet is formed with wedge shape.

For the THz spectral measurement, THz wave is generated from GaP based on non linear optical effect. We use Nd:YAG laser as a pumping light. Two near-infrared (NIR) beams are from Cr:Forsterite lasers, and we use two detectors of DTGS in a double beam configuration. Two NIR laser beams from Cr:Forsterite lasers are introduced to GaP, then THz wave is generated via the difference frequency generation method. The THz-wave path was purged with dry air to eliminate water vapour absorptions. Absorbance is calculated by Lambert-Beer law. For practical applications, the diffused reflection spectrum of natural copper oxide was measured. In reflection spectral measurements, 4K cooled Si bolometer was used as a THz detector. Samples are copper electric line with oxidized surface and not oxidized surface. THz wave induced to sample surfaces are separated into two directions. One THz wave is reflected at sample surfaces and the other is transmitted and reflected at the interface between an oxide film and a copper substance.

Figure 11(a) shows THz spectra of Cu_2O with various concentrations. One sharp absorption peak is appeared at 4.43 THz. Over wide frequency region from 2.2 to 4.2 THz, the broad band is observed. Following the background correction, these absorption bonds are split

with a Gaussian function fitting. For each band the intensity are plotted against sample concentrations in a log-log graph, as shown in Figure 11(b). It is apparent that the each integrated intensity increase as a function of sample concentration.
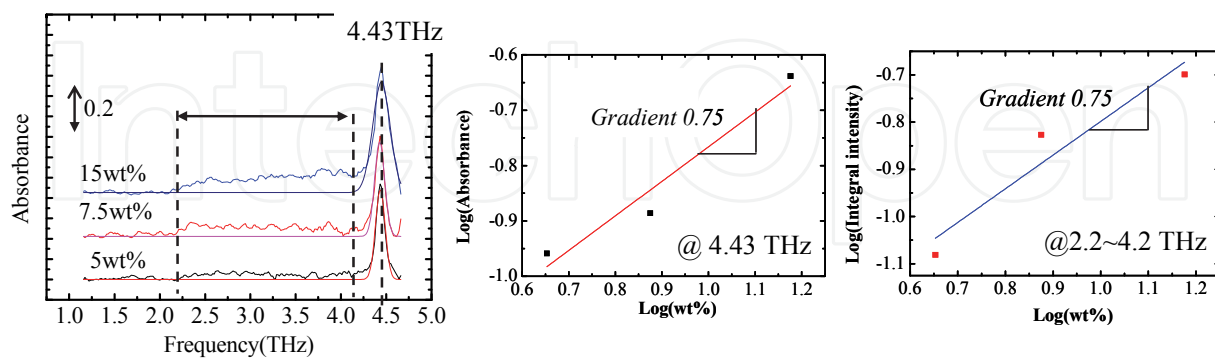

Fig. 11. THz spectra of Cu_2O with various concentrations at room temperature.

THz spectra of CuO are shown in Figure 12(a). A broad band is observed. The integrated intensity is plotted in Figure 12(b) as a function of sample concentrations in a log-log graph. This intensity increases against the concentration. The broad band is assigned to CuO. THz spectral feature of CuO is difference from that of Cu_2O.

Figure 13 shows THz spectra of copper oxalate. An asymmetric band is observed around 3.3 THz. The band is split into 3 peaks with a Gaussian function fitting. The peak positions are 2.7, 3.4, and 3.5 THz, respectively. For bands at 2.7 and 3.4THz, the intensities are increased as a function of sample concentration. That means the 2.7 and 3.4 THz bands are assigned to copper oxalate. But, for 3.5 THz band, the intensity is near constant regardless of sample concentrations. The 3.5 THz band is not due to the sample.
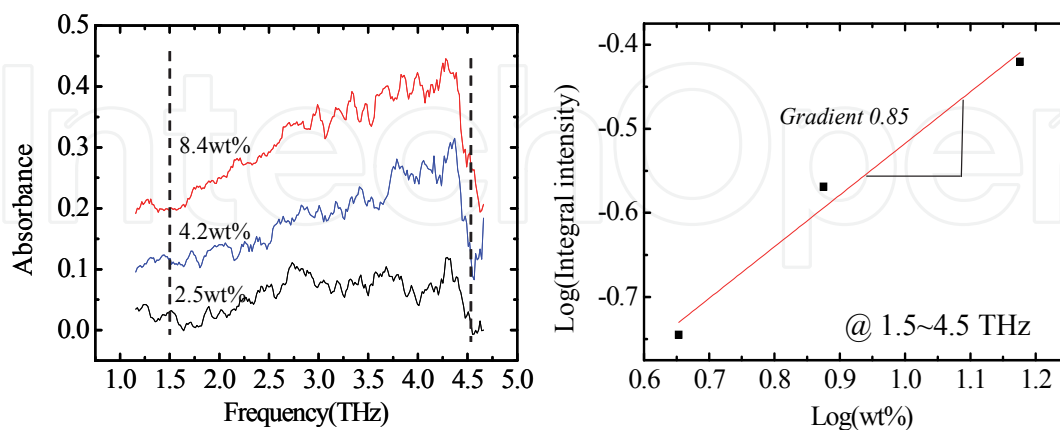

Fig. 12. THz spectra of CuO with various concentrations at room temperature.

Diffused reflection THz spectra of copper surface covered with oxide and without oxides were shown in Figure 14(a), respectively. In the region from 1.3~2.5 THz, the reflectance is

difference in each spectrum. The THz reflectance from the no oxide surface is larger than that from the oxide surface, which is attributable to the very thin surface oxide layer, even though the oxide layer thickness is very thin compared with the wavelength of THz wave. The difference is plotted at each frequency as an absorption spectrum of natural oxide, shown in Figure 14(b). The absorption band is split into 3 peaks with a Gaussian function fitting. The positions are 1.51, 1.77 and 1.95 THz, respectively. Every peak position is not in agreement with that of standard copper chemicals. This is due to the difference of composition ratio for Cu and O between the natural copper oxide and standard copper chemicals. The depth profiles of relative concentration are obtained on CuO, Cu and O by secondary ion mass spectroscopy (SIMS). Cs$^+$ primary ions at an energy of 5 keV were used. The ion incidence angle is 60 ° relative to the surface normal. The ion current was 100 nA and the beam was scanned across areas of 300 μm × 300 μm. To reduce the crater effect, the analysis beam with square of 90 μm was positioned in the center of sputter scan area. CuO was used to monitor the distribution of oxygen. The monitoring CuO$^-$ cluster leads to change of dynamic range with half order of magnitude around 3 μm. The depth profile indicates the thickness of the oxide layer was 3 μm. The O$^-$ yield is saturated so that the oxygen distribution is nearly uniform. Matrix effect affect on the Cu$^-$ yield. The difference of THz reflectivity is helpful for a non-destructive evaluation of the corrosion of metal surface. This result is one of killer applications of THz wave and greatly contributes in the field of non-destructive inspection for corroded metals, even covered with an insulating polyethylene.
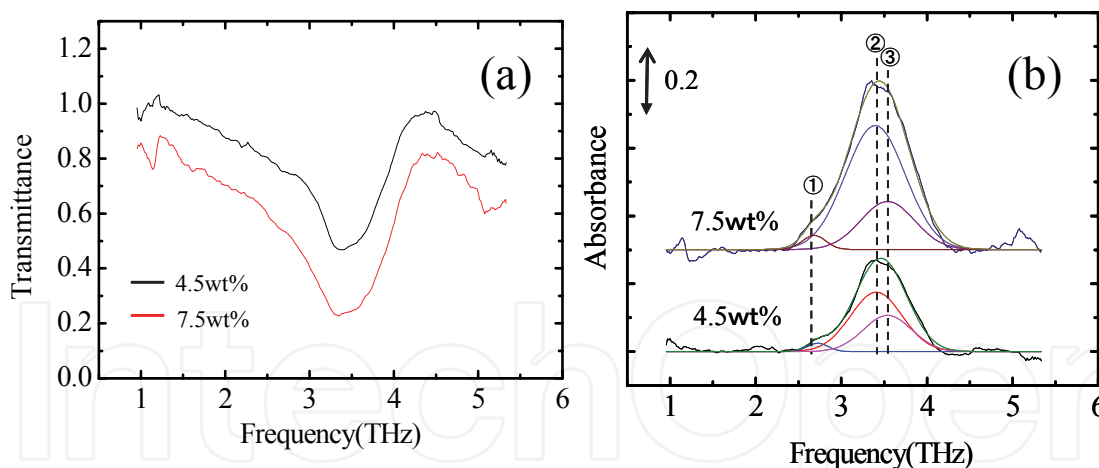

Fig. 13. THz spectra of Cu(COO)$_2$ · 1/2H$_2$O with various concentrations at room temperature.

For THz reflection spectroscopy, very thin surface oxide layer reveals serious difference on THz reflectivity at a specific frequency even when layer thickness is very thin compared with the wavelength of THz wave. This phenomenon contributes to detect the corroded surface of metals for non-destructive evaluation of corrosion. To realize such an evaluation, THz wave is the best, due to its high permeability for insulators and sensitive change of reflection intensity from metal surface even covered with insulators.
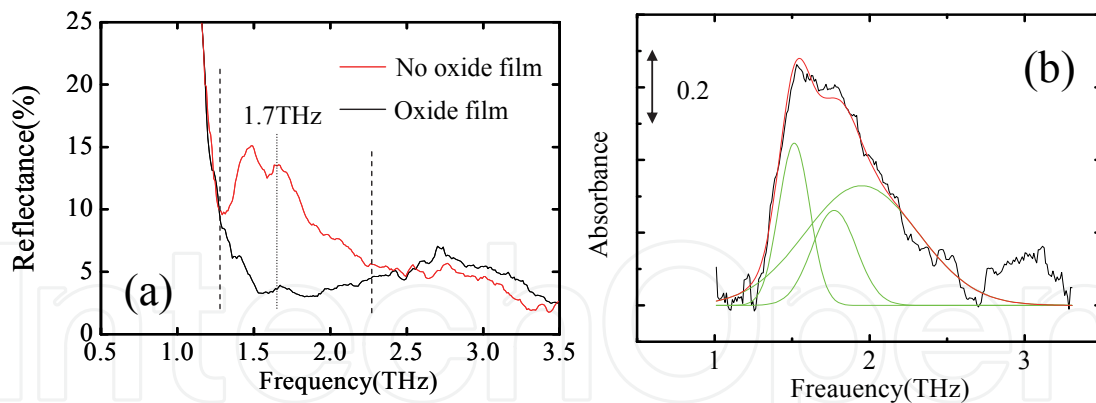
Fig. 14. THz spectra of copper surface covered with oxide and without oxides at room temperature.

5. Conclusion

Frequency-tunable terahertz (THz) wave pulse is generated by exciting a phonon-polariton mode in a GaP crystal, which are based upon non-collinear phase-matched different frequency generation (DFG) of nonlinear optical effect. We have developed a compact THz-wave generator using two small Cr:Forsterite lasers with single Q-switched Nd:YAG laser pumping. A Cr:Forsterite laser was constructed with diffraction gratings, by which the pulse duration and delay time of the Cr:Forsterite laser depend on Cr:Forsterite laser energy and the cavity length. The Cr:Forsterite laser energy was tuned using the optical alignment and pumping energy. Temporal overlap of two Cr:Forsterite laser pulses was realized at the GaP crystal. A single-frequency THz wave was generated at energy of 4.7 pJ around 2.95 THz using a 30-cm-long Cr:Forsterite laser system. The tunable range was approximately 0.3–7.5 THz.

The THz waves are located between radio waves and light waves. Thus, a THz wave has unique properties with high transparency for non-polarized materials such as with radio waves and easy handling as in the case of light. THz waves are expected to be a promising frequency for the non-destructive diagnosis of the interior of non-polarized materials. THz non-destructive diagnosis are possible for tensile strain in deformed polyethylene and metal conductor surfaces covered with insulating polyethylene.

6. References

[1] J. Nishizawa, "Semiconductor Maser", Japanese Patent 273217, April 1957.

[2] K. Suto and J. Nishizawa, "Low-threshold semiconductor Raman laser", *IEEE J. Quantum Electron.*, vol. 19, pp. 1251-1254 (1983).

[3] K. Suto, T. Kimura, J. Nishizawa, "Fabrication and characteristics of tapered waveguide semiconductor Raman laser", *IEE Proc.-Optoelectron*, vol. 143, pp. 113-118 (1996).

[4] T. Tanabe, K. Suto, J. Nishizawa, T. Kimura and K. Saito, "Frequency–tunable high-power terahertz wave generation from GaP", *J. Appl. Phys.*, vol. 93, pp. 4610-4615 (2003).

[5] T. Tanabe, K. Suto, J. Nishizawa, K. Saito, T. Kimura, "Tunable Terahertz Wave Generation in the 3- to 7-THz region from GaP", *Appl. Phys. Lett.*, vol. 83, pp. 237-239 (2003).

[6] T. Tanabe, K. Suto, J. Nishizawa, K. Saito, T. Kimura, "Frequency-tunable terahertz wave generation via excitation of phonon-polaritons in GaP", *J. Phys. D: Appl. Phys.*, vol. 36, pp. 953-957 (2003).

[7] K. Suto, T. Sasaki, T. Tanabe, K. Saito, J. Nishizawa, M. Ito, "GaP THz wave generator and THz spectrometer using Cr:Forsterite lasers", *Rev. Sci. Instrum.*, vol. 76, pp. 123109 1-3 (2005).

[8] J. Nishizawa, T. Tanabe, K. Suto, Y. Watanabe, T. Sasaki, Y. Oyama, "Continuous-wave frequency-tunable terahertz-wave generation from GaP", *IEEE Photo. Tech. Lett.*, vol. 18, pp. 2008-2010 (2006).

[9] B. B. Hu, M. C. Nuss, "Imaging with terahertz waves" *Opt. Lett.* vol. 20, pp. 1716-1719 (1995).

[10] D. M. Mittleman, M. Gupta, R. Neelamani, R. G. Baraniuk, J. V. Rudd, M. Koch, "Recent advances in terahertz imaging" *Appl. Phys. B* vol. 68, pp. 1085-94 (1999).

[11] B. Ferguson, X. -C. Zhang "Materials for terahertz science and technology" *Nature Mater.* vol. 1, pp. 26-33 (2002).

[12] K. Kawase, Y. Ogawa, Y. Watanabe, H. Inoue "Non-destructive terahertz imaging of illicit drugs using spectral fingerprints" *Opt Express* vol. 11, pp. 2549-54 (2003).

[13] J. Nishizawa, "Development of THz wave oscillation and its application to molecular sciences" *Proc. Jpn. Acad. Ser. B* vol. 80, pp. 74-81 (2004).

[14] M. Tonouchi, "Cutting-edge terahertz technology" *Nature Photo.* vol. 1, pp. 97-105 (2007).

[15] Y. Oyama, L. Zhen, T. Tanabe, M. Kagaya, "Sub-Terahertz Imaging of Defects in Building Blocks" *NDT & E Int.* vol. 42, pp. 28-33 (2009).

[16] J. Nishizawa, T. Yamada, T. Sasaki, T. Tanabe, T. Wadayama, T. Tanno, K. Suto, "Terahertz dichroism of MBBA liquid crystal on rubbed substrate" *Appl. Surf. Sci.* vol. 252, pp. 4226-29 (2006).

[17] T. Tanabe, K. Watanabe, Y. Oyama, K. Seo, "Polarization sensitive THz absorption spectroscopy for the evaluation of uniaxially deformed ultra-high molecular weight polyethylene" *NDT & E Int.* vol. 43, pp. 329-333 (2010).

[18] J. Nishizawa, T. Sasaki, T. Tanabe, N. Hozumi, Y. Oyama, Ken Suto "Single-frequency coherent terahertz-wave generation using two Cr:forsterite lasers pumped using one Nd:YAG laser" *Rev. Sci. Instrum.* vol. 79, p. 036101 (2008).

[19] A. Mooradian and G. B. Wright, "First order Raman effect in III–V compounds", *Solid State Commun.* vol. 4, pp. 431-434 (1966).

[20] V. G. Dmitriev, G. G. Gurzadyan, D. N. Nikogosyan, Handbook of Nonlinear Optical Crystals (Berlin: Springer) pp. 68-240 (1997).

[21] M. Tasumi, T. Shimanouchi, "Crystal Vibrations and Intermolecular Forces of Polymethylene Crystals" *J. Chem. Phys.* vol. 43, pp. 1245-58 (1965).

[22] M. Tasumi, S. Krimm "Crystal Vibrations of Polyethylene" *J. Chem. Phys.* vol. 46, pp. 755-766 (1967).

[23] K. Yamamoto, M. Yamaguchi, M. Tani, M. Hangyo, S. Teramura, T. Isu, N. Tomita, "Degradation diagnosis of ultrahigh-molecular weight polyethylene with terahertz time-domain spectroscopy" *Appl Phys Lett* vol. 85, pp. 5194-5196 (2004).

[24] R. P. Wool, R. S. Bretzlaff, B. Y. Li, C. H. Wang, R. H. Boyd, "Infrared and raman spectroscopy of stressed polyethylene " *J. Polym. Sci. B.* vol. 24, pp. 1039-1066 (1986).
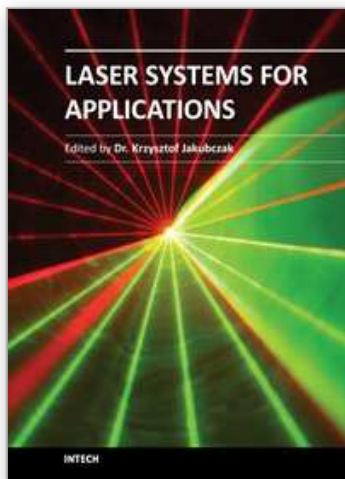
Laser Systems for Applications

Edited by Dr Krzysztof Jakubczak

This book addresses topics related to various laser systems intended for the applications in science and various industries. Some of them are very recent achievements in laser physics (e.g. laser pulse cleaning), while others face their renaissance in industrial applications (e.g. CO2 lasers). This book has been divided into four different sections: (1) Laser and terahertz sources, (2) Laser beam manipulation, (3) Intense pulse propagation phenomena, and (4) Metrology. The book addresses such topics like: Q-switching, mode-locking, various laser systems, terahertz source driven by lasers, micro-lasers, fiber lasers, pulse and beam shaping techniques, pulse contrast metrology, and improvement techniques. This book is a great starting point for newcomers to laser physics.

How to reference

In order to correctly reference this scholarly work, feel free to copy and paste the following:

INTECH
open science | open minds